Article

Spark Plasma Sintering of Nanostructured TiCrC Carbides Prepared via Mechanical Alloying

Mohsen Mhadhbi [1,*], İlker Emin Dağ [2,3], Barış Avar [2,3], Mohamed Khitouni [4], Frédéric Schoenstein [5], and Noureddine Jouini [5]

[1] Laboratory of Useful Materials, National Institute of Research and Physicochemical Analysis, Technopole Sidi Thabet 2020 Ariana, Tunisia; mohsen.mhadhbi@inrap.rnrt.tn (M.M.)
[2] Department of Nanotechnology Engineering, Zonguldak Bülent Ecevit University, Zonguldak 67100, Turkey; ilkeremin.dag@gmail.com (I.E.D.); barisavar@beun.edu.tr (B.A.)
[3] Department of Metallurgical and Materials Engineering, Zonguldak Bülent Ecevit University, Zonguldak 67100, Turkey; ilkeremin.dag@gmail.com (I.E.D.); barisavar@beun.edu.tr (B.A.)
[4] Department of Chemistry, Colleague of Science, Qassim University, Buraidah 51452, Saudi Arabia; khitouni@yahoo.fr (M.K.)
[5] Laboratory of Sciences of Processes and Materials, CNRS-UPR 3407, Paris 13 University, 93430 Villetaneuse, France; frederic.schoenstein@univ-paris13.fr (F.S.); nourredine.jouini@lspm.cnrs.fr (N.J.)
* Correspondence: mohsen.mhadhbi@inrap.rnrt.tn; Tel.: +21671537666

Abstract: In order to produce nanostructured $Ti_{0.9}Cr_{0.1}C$ powders, an elemental powder mixture of titanium, chromium, and graphite is milled in this work using a high-energy ball mill for various milling times. Microstructural characteristics such as crystallite size, microstrain, lattice parameter, and dislocation density are determined using X-ray diffraction (XRD). Mechanical alloying successfully produced nanocrystalline (Ti,Cr)C with an average crystallite size of 11 nm. This size of the crystallites is also directly verified using transmission electron microscopy (TEM). Scanning electron microscopy (SEM) was used to investigate the morphology of the samples. The novelty of this work is advancing the scientific understanding of the effect of milling time on the particle size distribution and crystalline structure, and also understanding the effect of the spark plasma sintering on the different properties of the bulks. Densified cermet samples were produced from the nanocrystalline powders, milled for 5, 10 and 20 hours by SPS process at 1800 degrees for 5 min under a pressure of 80 MPa. Phase changes of the produced cermets were examined according to XRD, SEM/EDX analyses. Significant amounts of Cr and Fe elements were detected, especially in the 20 h milled cermet. The bulk forms of the milled powders for 5 and 20 h had a relative density of 98.43 and 98.51 %, respectively. However, 5 h milled cermet had 93.3 HRA because of the more homogeneous distribution of the (Ti,Cr)C phase, the low iron content and high relative density. According to the 0.0011 mm/year corrosion rate, and 371.68 $k\Omega*cm^2$ charge transfer resistance obtained from the potentiodynamic polarization and EIS tests, the 20 h cermet was the specimen with the highest corrosion resistance.

Keywords: mechanical alloying; titanium carbide; spark plasma sintering; cermets; corrosion.

1. Introduction

Due to its exceptional qualities, including high hardness, high chemical stability, high melting point, strong resistance to abrasion, etc., titanium carbide (TiC) is a promising material that is frequently used for cutting tools [1]. In addition, TiC is employed in optics, electronics, and other fields. However, due to its wear resistance, corrosion resistance, higher temperature stability, and high hardness in comparison to TiC, titanium chromium carbide (TiCrC) is one of the wear-resistant materials [2-4].

In a prior paper [5], we investigated how milling affected the structural and microstructural evolution of (Ti,Cr)C nano-carbide. Chuev and Covalev [6] have looked into the impact of titanium's high-energy ball milling on the ratio of TiCX under reaction-diffusion in the Ti and C system. They demonstrated that non-stoichiometric $TiC_{0.4-0.5}$

Preprints (www.preprints.org) | NOT PEER-REVIEWED | Posted: 5 December 2022 doi:10.20944/preprints202212.0076.v1

carbides form after 3 min of milling while stoichiometric $TiC_{0.8-1.0}$ carbides form after 1 min. On the other hand, $(Ti_{0.88}W_{0.12})C$ nanopowder was made by Zhang et al. [7] using a carbothermal reduction-carbonization process in argon. The twin boundary structure and stacking defects of the powder particles were discovered. Moreover, starting with an elemental powder mixture of titanium, tungsten, and graphite, Bandyopadhyay et al. [8] produced nanocrystalline $Ti_{0.9}W_{0.1}C$ powders with a particle size of 11 nm after 8 hours of milling. On the other hand, by electrospinning (Ti,Zr)C solid solution nanofibers with polymeric precursors, Li et al. [9] created them. In comparison to TiC nanofibers, they discovered that the end product's oxidation temperature was increased. Other research has shown that solid solution ceramics and the addition of Mo and Co to the TiC matrix help to improve the oxidation resistance [10, 11].

The microstructure and mechanical characteristics of (Ti,W)C cermets produced by spark plasma sintering were studied by Wang et al. When compared to TiC, the cermets had superior mechanical properties, with Vickers hardness of 18.42 GPa, a flexural strength of 1340.90 MPa, and fracture toughness of 11.96 $MPam^{1/2}$ [12]. Due to the abundance of titanium resources in the crust, TiC is produced at a comparatively low cost. Additionally, Zhang et al. [13] used arc melting to create bulk solutions of Zr, Hf, and Ta carbides. The carbides had good oxidation resistance even at 1000 °C, according to thermogravimetric measurements.

Many metallurgical techniques are used to create metal carbides, including MA, a straightforward method for processing powder that can produce both equilibrium and non-equilibrium phases. Powder particles are cold-welded, fractured, and re-welded in this process. However, using MA to create powdered components, nanocrystalline metal carbides could be easily created [14, 15]. The main benefit of MA is the production of a fine, homogenous, nanostructured powder that may be molded and hardened in accordance with specific conditions using the traditional powder metallurgy technique [16]. Because there are significant temperature changes between the alloying processes, MA overcomes flaws in traditional methods including evaporation and undesirable separation [17]. In a non-conventional and non-equilibrium mode of synthesis, the MA technique may be employed to produce nanocrystalline and amorphous alloys with favorable structural and mechanical properties [18]. MA provides substantial technical advantages over traditional approaches, such as low processing temperature, simple optimization, and low cost [19].

Using starting individual elements, nanostructured $Ti_{0.9}Cr_{0.1}C$ powders were synthesized in this study using MA followed by SPS that had successfully optimized. The innovative aspect of this work is that the MA of TiCrC nano-carbides followed by SPS is reported for the first time. The properties of the milled and consolidated samples are investigated.

2. Materials and Methods

2.1. Preparation of TiCrC Cermets by Mechanical Alloying (MA) and Spark Plasma Sintering (SPS)

A mixture of elemental Ti (40 m, 99.9%, Pro-labo), carbon (5 m, 99.9%, Fischer scientific), and chromium (100-300 m, 99.9%, ACROS) powders was enclosed in a stainless steel vial (45 mL in capacity) with five stainless steel balls (15 mm in diameter and 14 g in mass) to prevent oxidation. Figure 1 shows SEM images of the raw powders (Ti, Cr, and graphite). The injected chock power (5.19 W/g) is maintained constant. The ball-to-powder weight ratio (BPR) was 70:1. The balls and vials were cleaned in an ultrasonic bath with acetone as the cleaning agent prior to experimentation. Utilizing a high-energy planetary ball mill, an MA operation lasting up to 20 hours was performed at room temperature. Figure 2a shows a schematic illustration of the MA process. In order to prevent the temperature within the vial from rising, the milling operation was stopped for 15 minutes after every 30 minutes. The powder was removed from the vial that had been opened in the glove box after each specified milling period. SPS was car-

Preprints (www.preprints.org) | NOT PEER-REVIEWED | Posted: 5 December 2022 doi:10.20944/preprints202212.0076.v1

ried out by 5155 SYNTEX apparatus at 1800 °C for 5 min under a pressure of 80 MPa, as seen in Figure 2b.

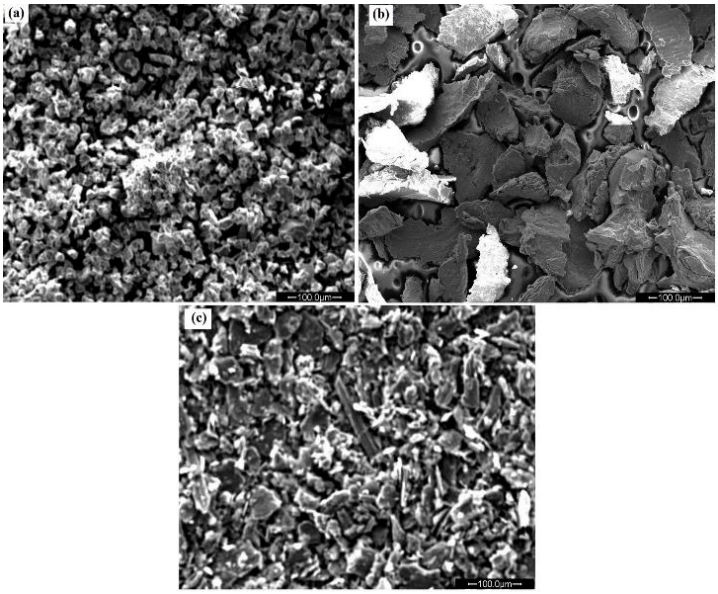

Figure 1. SEM images of starting powders of (a) Ti, (b) Cr, and (c) graphite.

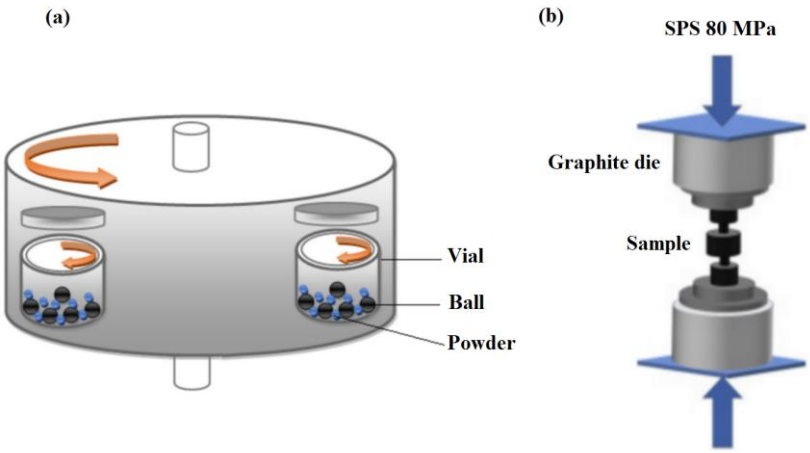

Figure 2. Schematic illustration of (a) MA process, and (b) SPS process.

2.2. Materials Characterization

Using a Panalytical XPERT PRO MPD diffractometer with CuK_α radiation (λ = 0.15418 nm) operating at 45 kV and 40 mA, the structural changes of the powdered cermets at various MA durations ranging from 30 min to 20 h, and the densified cermets for 5, 10, and 20 of milling obtained after SPS were studied. Two-theta was recorded with a step of 0.02 between 20 and 80 degrees. Using a TEM with a model FEI Tecnai G2 high-resolution operating at 200 kV and 1.9 Å spatial resolution, the samples' microstructure was characterized. A few drops of the ethanol-based powder suspension were then put onto a copper microgrid after the powders had been prepared by being dispersed with the use of ultrasound.

The densified cermets obtained after the SPS were sanded up to 1200 grit sandpaper and polished with 1 μm colloidal silica. After polishing the pellet samples, scanning electron microscopy (SEM, Tescan, MAIA3 XMU) equipped with energy-dispersive

Preprints (www.preprints.org) | NOT PEER-REVIEWED | Posted: 5 December 2022 doi:10.20944/preprints202212.0076.v1

X-ray spectroscopy (EDX, Oxford Xmax 50) was used to analyze the microstructure of the manufactured cermets. Archimedes' principle was used to perform density tests on the pellets. The experimental densities obtained from these tests were compared to the theoretical density values, and total porosity was determined. With a preload of 10 kg and a constant load of 60 kg, the standard Rockwell device was used to test the hardness of the cermets.

2.3. XRD Analysis of the Powdered Cermets

The phases were identified in the current investigation using the High Score Plus software based on the ICDD PDF2 database, and the crystallite size was calculated from acquired diffraction data using the FullProf program [20] employing the Rietveld powder structure refinement analysis of X-ray powder diffraction step scan data [21-28] to produce the refined structural and microstructural parameters. The pseudo-Voigt analytical function was the profile chosen for the refining.

The most generally used criteria for assessing the strength of the Rietveld refinement fit are the reliability factors R_{wp} (weighted residual error), R_{exp} (expected error), R_B (Brag factor), and χ^2 (goodness factor). Additionally, lower error indices values show a better fit between the computed (I_c) and observed (I_o) powder diffraction patterns (if $\chi^2 > 1$, we can infer that the structure is highly refined). To evaluate the refining quality, a graphical perspective of fit is required. In our work, the Rietveld analysis has predicted quantitative assessments of several phases in unmilled and milled materials. To examine the microstructural evolution of $Ti_{0.9}Cr_{0.1}C$ powders during MA, the Rietveld method, one of the best methods for quantitative phase analysis, was employed in this study. Refined experimental data is used to determine microstrain, crystallite size, lattice parameter, and dislocation density.

In addition to grain boundaries, which are formed by plastic deformation brought on by MA, dislocations are the main crystal defects. Based on XRD measurements, the dislocation density is computed as [29]:

$$\rho = \frac{2\sqrt{3}\langle \varepsilon^2 \rangle^{1/2})}{Db} \quad (1)$$

where b is the Burgers vector of dislocations and D is the average size of coherent domains of diffraction. For the FCC materials subjected to cold plastic deformation, the slip of dislocations occurs on {111} planes in <110> directions. The Burgers vector for $Ti_{0.9}Cr_{0.1}C$ carbide in direction [111] is presented by a/n× [110]. However, its value is given by:

$$\frac{a}{n}\sqrt{(h^2+k^2+l^2)} = \frac{a}{n}\sqrt{2} \quad (2)$$

where a is the lattice parameter of $Ti_{0.9}Cr_{0.1}C$ carbide, which changes with milling time and h, k, and l are the Miller indices.

2.4. Electrochemical Measurements

The electrochemical workstation Gamry Interface 1010E potentiostat/galvanostat was employed to carry out the potentiodynamic polarization studies on the polished samples. The experiments were conducted using a three-electrode system, with (Ti,Cr)C cermet, graphite rods, and Ag/AgCl electrodes serving as the working electrode (WE), counter electrode (CE), and reference electrode (RE), respectively. 3.5 wt.% NaCl solution was used for electrochemical experiments and before each test, immersion was carried out for 900 seconds to stabilize the open circuit potential (OCP). For all measurements, the working electrode surface area was adjusted at 0.16 cm^2. Tafel polarization experiments were conducted at a scan rate of 10^{-3} V/s from -0.5 V vs OCP to a final potential of 0.5 V vs OCP. Calculating corrosion resistance using Tafel curves requires finding the

Preprints (www.preprints.org) | NOT PEER-REVIEWED | Posted: 5 December 2022 doi:10.20944/preprints202212.0076.v1

corrosion current density, intersecting it with the tangents drawn to the anodic and cathodic curves, and then using the formula in the ASTM G102 standard provided in Eq. (3) [30]:

$$CR = K_1 \frac{i_{corr}}{\rho} EW \tag{3}$$

where K_1 is a constant equal to 3.27×10^{-3} (mm g/μA cm yr), i_{corr} is the corrosion current density (μA/cm^2), EW is the equivalent weight of the material, ρ is density (g/cm^3), and CR is the corrosion rate in (mm/year). Additionally, the polarization resistance may be calculated using the Stern-Geary equation provided in Eq. (4)[31] employing corrosion current density, anodic Tafel slopes, and cathodic Tafel slopes.

$$i_{corr} = \frac{1}{2.303 R_p} \left(\frac{\beta_a x \beta_c}{\beta_a + \beta_c} \right) \tag{4}$$

Here, i_{corr}, R_p and β_a, β_c denote corrosion current density (A/cm^2), polarization resistance (ohms.cm^2), and anodic, cathodic Tafel slopes (volts/decade). Equivalent weights of cermets were calculated from metallic elemental ratios as in the study [32], and corrosion rates were determined from Eq. (3). Likewise the electrochemical impedance spectroscopy (EIS) tests were performed with 10 mV sinusoidal wave amplitude between 10^5 Hz and 10^{-1}Hz, with a three-electrode system and working electrode area stayed same with Tafel experiments.

3. Results and Discussions

3.1. Characterization of $Ti_{0.9}Cr_{0.1}C$ powders prepared via MA

Figure 3 displays the $Ti_{0.9}Cr_{0.1}C$ powders' XRD patterns before and after various milling times (0, 0.5, 1.5, 3, 5, 10, 15, and 20 h). As can be observed, the unmilled powder mixture's XRD pattern exhibits all of the expected Bragg peaks for the initial elements. The un-milled sample consists of Ti with two different allotropic structures: hexagonal close-packed (hcp) and body-centered cubic (bcc), Cr with bcc structure, and C with hexagonal structure. Nine Bragg peaks are visible in the Ti phase, and the remaining peaks belong to both the Cr and C phases. Only the Ti and Cr Bragg peaks remained after 30 minutes of milling due to a drop in the intensity of the graphite phase-corresponding Bragg peaks. After one and a half hours of milling, only the Ti and Cr Bragg peaks of the graphite remained. A new disordered solid solution begins to emerge as a result of the slow removal of Cr Bragg peaks and the disappearance of C Bragg peaks. After 3 hours of milling, the Cr Bragg peak at 45° totally vanished, and a new phase of (Ti,Cr)C with a structure resembling FCC NaCl appeared. The wear of the milling medium has also resulted in the appearance of a new Bragg peak connected to the iron (Fe) phase at the same time. There are just the (Ti,Cr)C and Fe Bragg peaks between 5 and 20 hours of milling. It was observed that the longer milling times had a significant impact on the Bragg diffraction peaks' broadening and intensity. Additionally, a small shift in the location of the Bragg diffraction peaks to larger 2-angle values is seen. This demonstrates how the solid solution of (Ti,Cr)C with nanostructures formed. Ghosh and Pradhan thus revealed the same phenomena [16]. We can infer from these MA settings that the creation of Ti0.9Cr0.1C is fully complete after 5 hours of milling and that, thereafter, an increase in MA time beyond 5 hours results in particle refinement with the preservation of the nanometric scale.

Preprints (www.preprints.org) | NOT PEER-REVIEWED | Posted: 5 December 2022 doi:10.20944/preprints202212.0076.v1

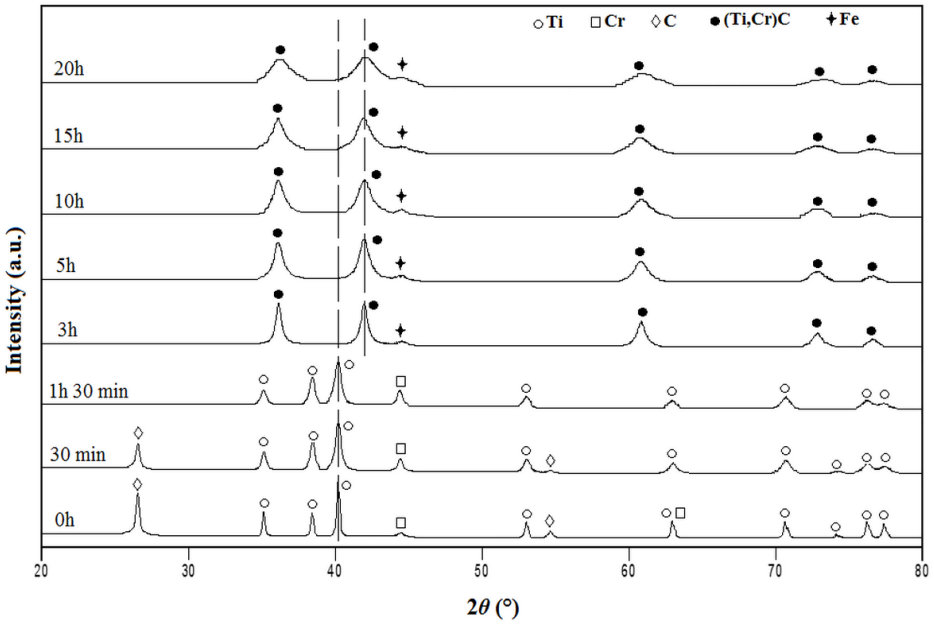

Figure 3. XRD patterns of $Ti_{0.9}Cr_{0.1}C$ powders before and after different milling times.

An example of a Fullprof software fit of the XRD pattern of the $Ti_{0.9}Cr_{0.1}C$ powders produced after 20 hours of MA is shown in Figure 4. The figure shows that the estimated and observed patterns are in excellent agreement. Additionally, the picture makes it quite evident that Cr substitutes Ti in the matrix TiC.

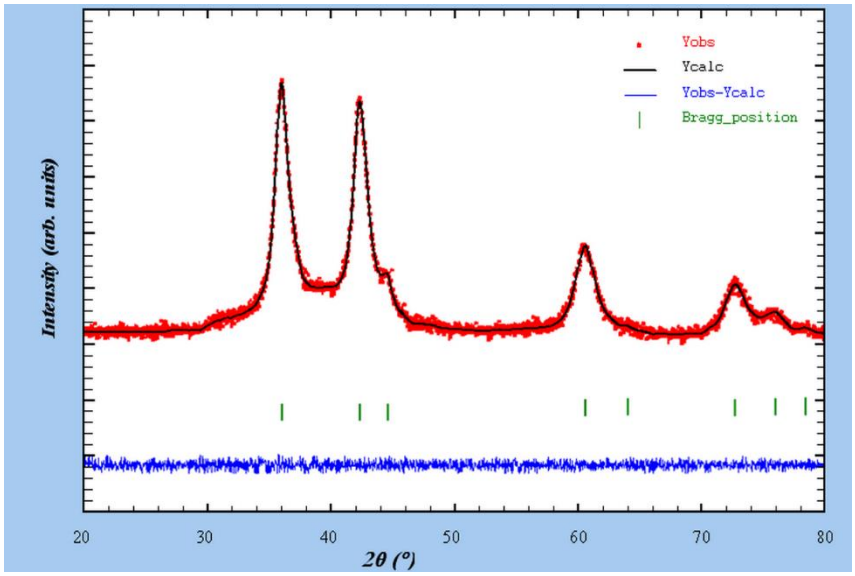

Figure 4. Example of Fullprof program fit of the XRD pattern of the $Ti_{0.9}Cr_{0.1}C$ powders obtained after 20 h of MA.

Using Rietveld structure analysis of the full pattern fitting structure refinement in factor of widening peaks, Figure 5 illustrates the variation of crystallite size and microstrain components as a function of milling time. Typically, the crystallite size and microstrain have an impact on the peak broadening of the diffraction profile. The change in crystallite size of the $Ti_{0.9}Cr_{0.1}C$ powders as a function of milling time is depicted in Figure 5a. It was discovered that as the MA time increased from 3 to 20 h, the crystallite size decreased from 22 to 11 nm (Figure 5a). The size distribution continuously decreases toward a lower value (11 nm) during MA. This suggests that MA causes particle fracturing and cold welding, which leads to the development of ductile-ductile systems.

Preprints (www.preprints.org) | NOT PEER-REVIEWED | Posted: 5 December 2022 doi:10.20944/preprints202212.0076.v1

According to Amini et al. [33], the balance between the increasing dislocation density and the recovery controlled by the annihilation of the dislocations is what causes the decrease in crystallite size. Additionally, several researchers [34-37] claimed that the plastic deformation of particles during the MA process could account for the reduction in particle size.

The microstrain variation of the $Ti_{0.9}Cr_{0.1}C$ powders as a function of milling duration is depicted in Figure 5b. With an increase in MA time from 3 to 20 hours, the microstrain increases from 0.14 to 1.35%. Additionally, it has been noted that the microstrain value rises steadily with rising MA time and practically remains constant for increasing MA time up to 20 h. Microstrain that is rising in nature continues until $Ti_{0.9}Cr_{0.1}C$ is fully formed. The presence of crystallite defects created during MA, according to Kamrani et al. [38], can be the cause of the rise in micro-strain. In fact, according to Zaara et al. [39], the increase in microstrain can be attributed to internal microdeformation and mechanical distortion. Therefore, Talischi and Samadi [40] observed that the additional dislocations inside particles introduced by a prolonged MA duration can account for the increase in microstrain. According to Ahmad et al. [41], the decrease in alloying element dissolution and reinforcement in the matrix over a longer MA time may be the cause of the rise in microstrain. Furthermore, the total metallic alloys produced by the MA process exhibit the behavior of decreasing crystallite size and increasing microstrain with increasing milling time [42]. In fact, the increase in surface temperature of the powders over longer MA times could account for the stable state of the crystallite size and microstrain attained after 15 h of MA [43].

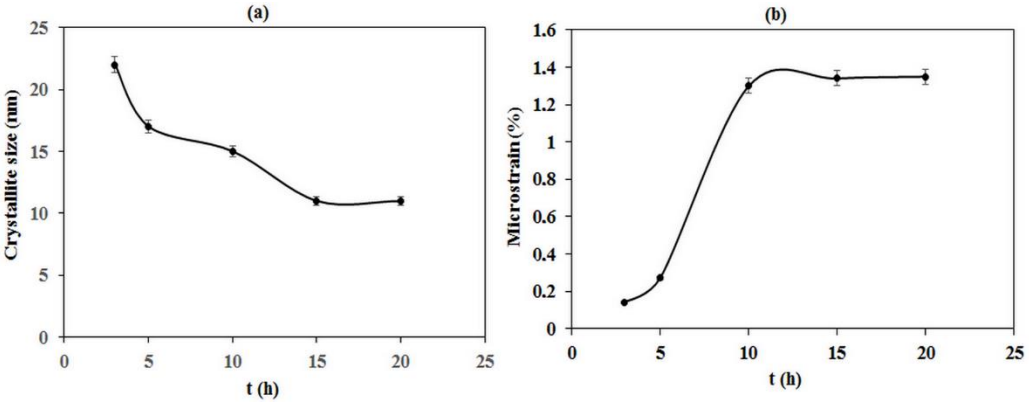

Figure 5. Variation of: (a) the crystallite size and (b) the microstrain of $Ti_{0.9}Cr_{0.1}C$ powders against the MA time.

The variation of the $Ti_{0.9}Cr_{0.1}C$ powders' lattice parameter as a function of milling time is depicted in Figure 6. The Rietveld method was used to determine the lattice parameter values. According to observation, the lattice parameter slowly decreases when the MA time is changed from 3 to 5 h. Between 5 and 20 hours, MA advances significantly before drastically reducing to a value of 0.42949 nm. This decrease is the result of Ti being substituted by Cr, which results in the formation of $Ti_{0.9}Cr_{0.1}C$ nano-carbide. The decrease in the lattice parameter of TiC following MA may be related to the compressive stress created in the MA mechanism to fracture into tiny nano-fragments, according to Ghosh and Pradhan [16]. The decrease in lattice parameter was in fact explained by Matula et al. [44] by the combination of cold welding and particle growth throughout the MA process. MA titanium alloys also show a similar behavior [45-47].

Preprints (www.preprints.org) | NOT PEER-REVIEWED | Posted: 5 December 2022 doi:10.20944/preprints202212.0076.v1

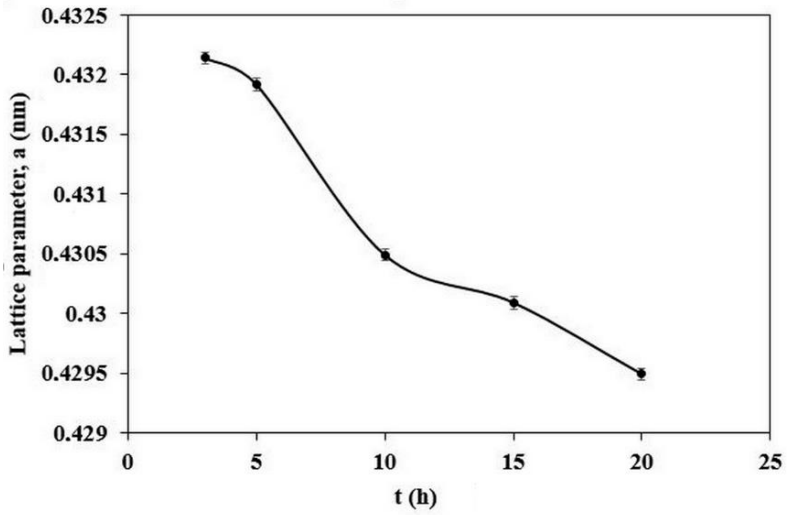

Figure 6. Variation of the lattice parameter of $Ti_{0.9}Cr_{0.1}C$ powders against the MA time.

The variation in dislocation density of the $Ti_{0.9}Cr_{0.1}C$ powders as a function of milling time is depicted in Figure 7. It is shown in the figure that as MA time increases from 3 to 20 hours, the dislocation density increases from 0.44111×10^{16} to 0.43022×10^{16} m^{-2}. The dislocation density does slightly rise at the MA between 15 and 20 h, as can be shown. The improvement in structure can explain this increase. $Fe_{70}Ni_{12}B_{16}Si_2$ alloy that had been milled for 150 hours also exhibited a similar tendency [39]. But it's clear that the MA time has a significant impact on dislocation density. The interaction of $Ti_{0.9}Cr_{0.1}C$ nanoparticles with dislocations, which restricts the motion of dislocations, can be used to explain the increase in dislocation density by extending the MA time.

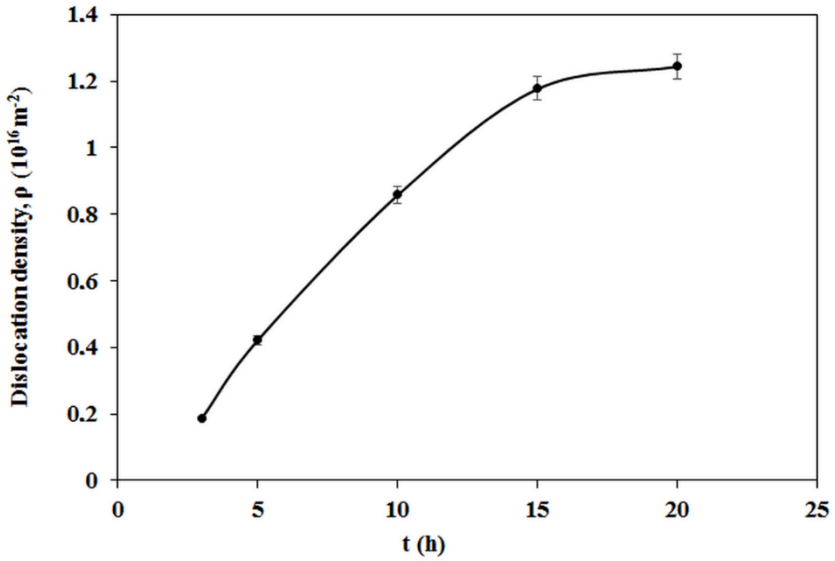

Figure 7. Variation of the dislocation density of $Ti_{0.9}Cr_{0.1}C$ powders against the MA time.

The images of $Ti_{0.9}Cr_{0.1}C$ powders MA for 20 h in various magnifications are shown in Figure 8(a-d) using high-resolution electron transmission microscopy (HRTEM). Figures 8a and 8b show TiCrC agglomerated powders with various nanoscale particle sizes. Amorphous (clear) and crystallizing (dark) regions can be seen in the $Ti_{0.9}Cr_{0.1}C$ powder particles in Figure 8c, which are spherical in shape and around 15 nm in size. A powder TiCrC particle with a size of around 15 nm is shown in Figure 8d. Reticular planes are present. The calculated interplanar spacing, obtained from Figure 8d, is equal to 0.242 nm, which corresponds to the (111) plane and indicates that the cubic $Ti_{0.9}Cr_{0.1}C$ phase

Preprints (www.preprints.org) | NOT PEER-REVIEWED | Posted: 5 December 2022 doi:10.20944/preprints202212.0076.v1

fully formed in the 20-hour MA sample. The indexed selected area electron diffraction (SAED) pattern shown in Figure 8e demonstrates the presence of only the cubic $Ti_{0.9}Cr_{0.1}C$ phase in the 20-hour MA sample. The figure clearly demonstrates the presence of broad, continuous diffraction rings. As a result, TEM analyses support XRD analyses in terms of the sample's collection after 20 hours of MA.

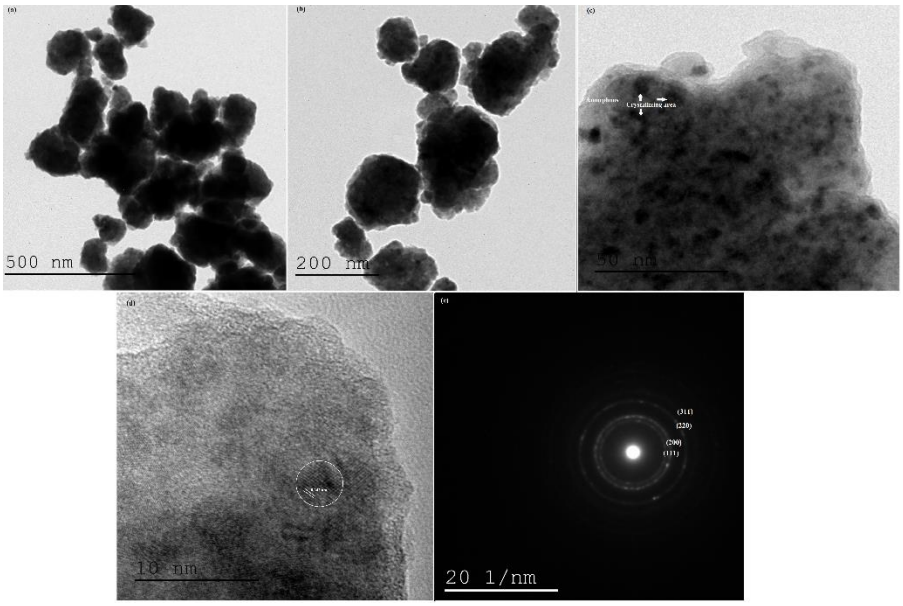

Figure 8. HRTEM images of $Ti_{0.9}Cr_{0.1}C$ powders MA for 20 h in different magnifications: (**a**) 500 nm, (**b**) 200 nm, (**c**) 50 nm, and (**d**) 10 nm. (**e**) Indexed SAED pattern.

As shown in Figure 9, during the MA process, a lot of iron (Fe) from the milling medium was incorporated into the inner of the powders and then enclosed by them. Additionally, the interaction between ball-to-wall and ball-to-ball collisions is responsible for the recurrent fracturing, welding, and rewilding of particles that happened during the MA process [48, 49].

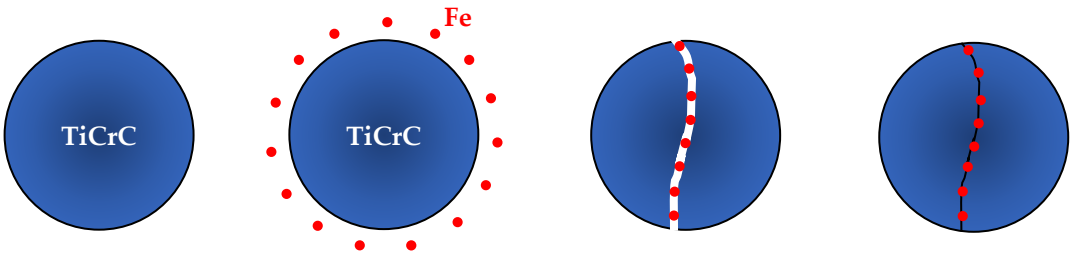

Figure 9. Schematic of the iron distribution into the inner of TiCrC powders during MA.

3.2. Characterization of bulk samples obtained by SPS

XRD results of the spark-plasma sintered samples produced from different milling time durations are presented in Figure 10. The XRD patterns of all three densified cermets exhibited the diffraction peaks corresponding to cubic (Ti,Cr)C phase (ICSD ref. code 98-005-3106), and cubic α-Fe phase (ICSD ref. code 98-018-0970), which is similar to XRD results of the as-milled (3-20 h) powders, as seen in Figure 11. However, the chromium carbide phases as hexagonal Cr_7C_3 (ICSD ref. code 98-005-2289), and orthorhombic Cr_3C_2 (ICSD ref. code 98-015-1477) phases were formed in the duration of the SPS process. According to the finding of Kunrath et al. [50] on TiC-Cr_3C_2 composites, the applied heat

Preprints (www.preprints.org) | NOT PEER-REVIEWED | Posted: 5 December 2022 doi:10.20944/preprints202212.0076.v1

treatment led to the precipitation of Cr_3C_2 from the low-chromium solid solution (Ti,Cr)C. In addition, with increasing milling time, the (Ti,Cr)C peak at around $2\theta \approx 36^{\circ}$ shifted to a higher angle as shown in the local magnification of Figure 10. This can be attributed to the change in the stoichiometry between the carbides [50]. This is also supported by the XRD results of the as-milled powders, where the Cr dissolves into the TiC, and forms the (Ti,Cr)C solid solution. Hence, the Cr_7C_3 phase transformed into Cr_3C_2 in the 20 h milled cermet after SPS. Meanwhile, the hexagonal graphite phase (ICSD ref. code 98-007-6767) was observed in the densified cermets due to the decomposition of the carbides to form free carbon during sintering.

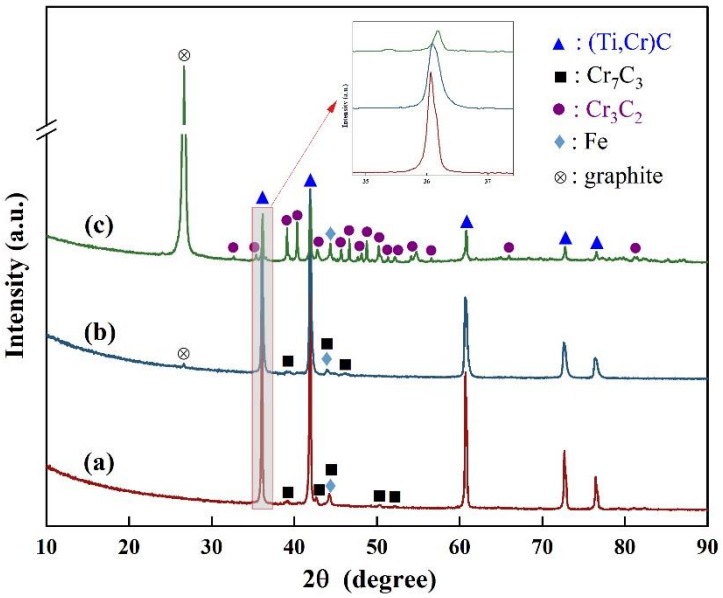

Figure 10. XRD patterns of the (a) 5 h, (b) 10 h, and (c) 20 h milled TiCrC samples after SPS.

Figure 11 illustrates the SEM images in backscattered electron (BSE) mode as well as their EDX mapping analysis. Figure 11a presents the microstructure of the 5 h milled sample. The dark areas in this image represent solid solution agglomerated graphite that has been decomposed from titanium and chromium carbides. While the gray region (TiCr) has a uniform distribution of the C phase, a few bright regions exhibit Cr-rich carbide. A minor quantity of Fe in the 5 h milled sample also showed up in some Cr-rich regions [51-53]. Figure 11b depicts the EDX mapping of the BSE-SEM image of the 10 h milled sample manufactured with SPS. When the images are compared, it becomes clear that the black zones are the agglomerated graphite that has been separated from (TiCr)C as in Figure 11a, whereas the gray areas in the BSE image consist of TiC. The Cr-rich carbide phase makes up the bright white areas. In addition, almost all Fe is located in the white region rich in Cr. This can be explained by the dissolution of iron, which is included in the powders as an impurity, with the increase of the milling time. Figure 11c shows four specific regions in the BSE-SEM image of the 20 h milled sample produced by SPS. As in previous images, graphite is visible in the black sections, while TiC is present in the gray parts. The white region, which is quite high compared to other samples, shows CrC with quite a lot of iron. The dark gray region denotes the chromium carbide phases, which have nearly zero TiC and less iron than the whiter area. According to the XRD results, the 20 h milled sample had the greatest iron concentration.

Preprints (www.preprints.org) | NOT PEER-REVIEWED | Posted: 5 December 2022 doi:10.20944/preprints202212.0076.v1

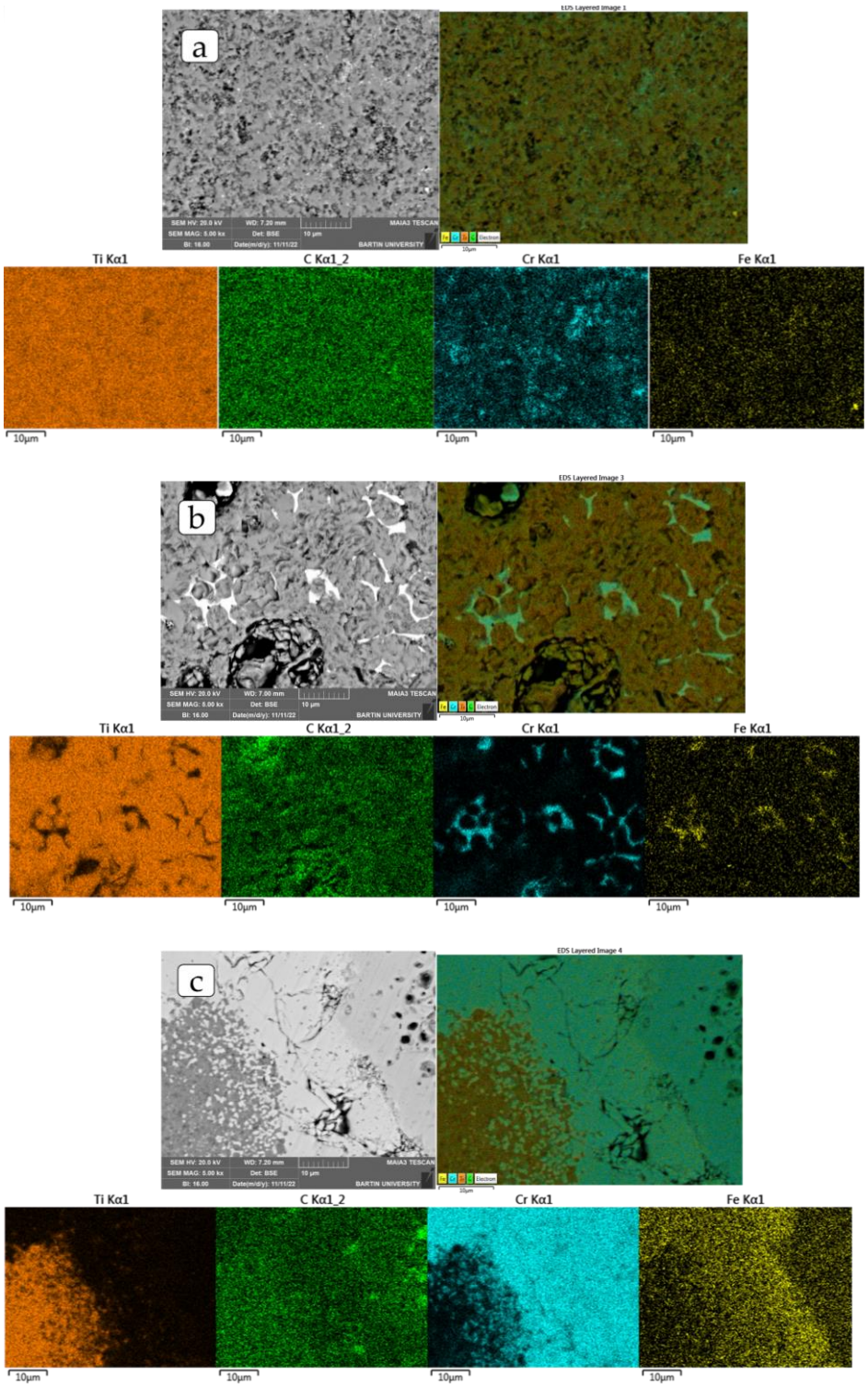

Figure 11. BSE-SEM and EDX-mapping images of the cermets by SPS for different milling times; (a) 5 h, (b) 10 h, and (c) 20 h.

The cermets' densities and hardness values were determined by the Archimedes test and Rockwell A test, depicted in Table 1. The porosities are also shown in accordance with the density values. Density and hardness values are similar in pellets that are milled for 5 and 20 hours, while these are higher than that of a pellet sample for 10 h of milling. The powders may have been coarsened and cold-welded as a result, lowering the manufacturing density. Once more, it is evident from the hardness data that the bulk structures of the powders milled for 5 and 20 hours consist of average hardness values near to

 doi:10.20944/preprints202212.0076.v1

one another. The hardness value of the 10 h milled sample is, like the density, significantly lower than that of the other bulk structures. Although the hardness of the powders milled for 10 h was found to be around 83.2, the average hardness values of 93.3 and 91.5 HRA for the bulk structures milled for 5 and 20 hours are close to those in the literature [54, 55]. The low hardness of the milled bulk structure for 10 h of milling can be attributed to the low density. In spite of its high density, the reduced hardness for the 20 h milled sample may be explained by an increase in the ratio of iron, a soft metal, as seen in the SEM-EDX and XRD results.

Table 1. Density and macrohardness values of the produced cermets.

Sample	Density (g/cm^3)	Relative density (%)	Rockwell Hardness (HRA)
5 h	5.029	98.43	93.3 ± 0.3
10 h	4.452	87.14	83.2 ± 1.7
20 h	5.033	98.51	91.5 ± 0.4

Tafel polarization curves, Nyquist plots, and electrical equivalent circuits are demonstrated in Figure12, and the results of electrochemical corrosion tests are shown in Table 2. All cermets indicated a very low corrosion rate. This is due to the strong corrosion resistance of carbides of titanium and chromium. It can be clearly comprehended that 10 h milled cermet has the highest corrosion rate among all. The solubility of the Cr element in the TiC matrix increases as a result of the increase in the milling time of the powder samples along with the strain-enhanced solubility. Although it is anticipated that an increase in the Cr ratio will reduce the rate of corrosion, the pores that develop due to the low density in particular act as corrosion zones and reduce corrosion resistance by boosting the surface area in contact with the solution, and the increase in porosity prevents the Cr_2O_3 layer from being continuous and hastens its deterioration [32, 56-59]. The lowest corrosion rate and maximum polarization resistance was obtained in 20 h milled cermet, as illustrated in Table 2. This is related to the fact that the increase of Cr_3C_2 phase whose solubility rises with milling time according to XRD and SEM/EDX results and the oxide of chromium preserves materials from being corrode [57]. Impurities from the stainless-steel vial may also be a contributing factor in the rise of iron and chromium elements in the characterization results. The corrosion resistance was also assessed using the EIS tests in addition to the Tafel polarization tests. The Nyquist plots in Figure 12b were fitted using the EC-lab program using the three-element circuit model. In this circuit model, Q_{ct}, the double layer constant phase element, R_{ct}, the charge transfer resistance, and R_s, the solution resistance. The strong corrosion resistance is closely correlated with the high charge transfer resistance [55, 57-60]. So, considering this as it can be seen in Table 2, and Figure 12b, the corrosion resistance degree of the pellet's in EIS tests is 20 h > 5 h > 10 h.

Preprints (www.preprints.org) | NOT PEER-REVIEWED | Posted: 5 December 2022 doi:10.20944/preprints202212.0076.v1

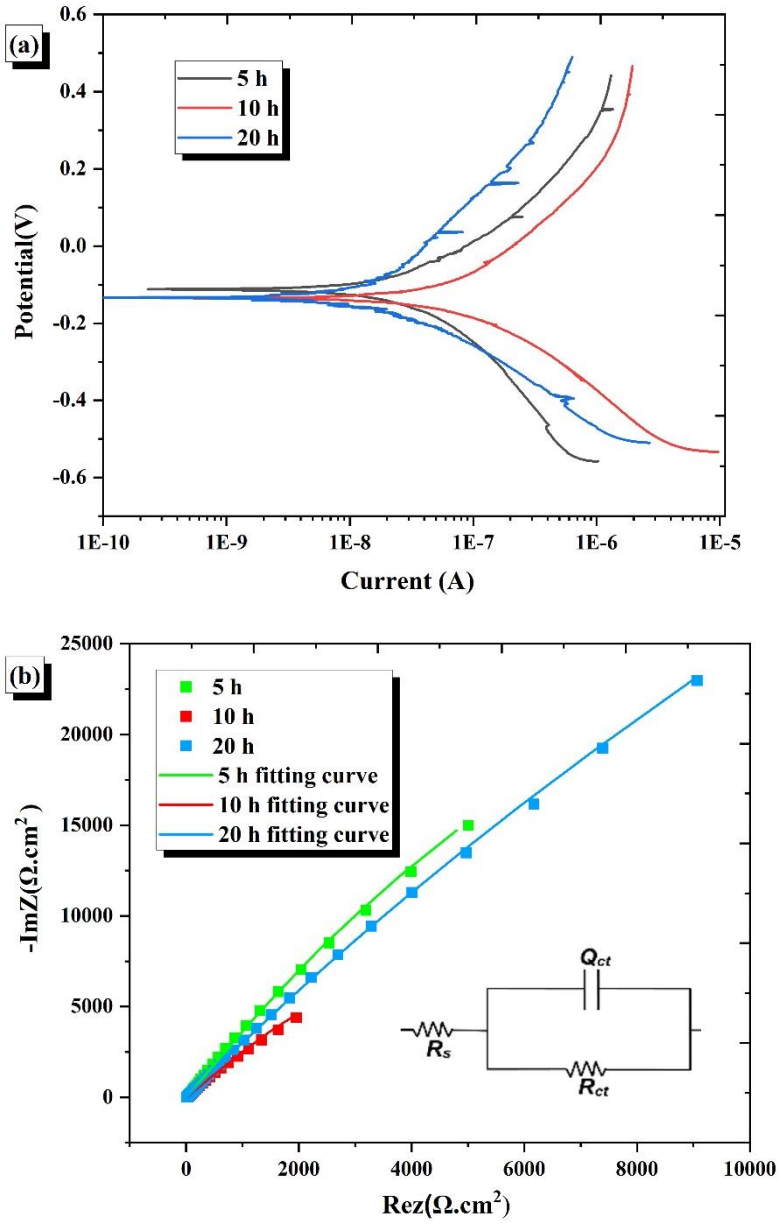

Figure 12. (a) Potentiodynamic polarization results of cermets, and (b) Nyquist plots of EIS results and equivalent circuit used for fitting.

Table 2. Electrochemical test results of the produced cermets.

Sample	E_{corr} (V)	i_{corr} (μA/cm²)	BetaA (V/decade)	BetaC (V/decade)	CR (mm/year)	R_p (kΩ*cm²)	R_{ct} (kΩ*cm²)
5 h	-0.112	0.2742	0.2819	0.3295	0.00236	240.57	302.24
10 h	-0.135	0.5654	0.3189	0.2132	0.00487	98.12	128.99
20 h	-0.133	0.1270	0.3698	0.1685	0.00110	395.63	371.68

5. Conclusions

In this study, it is shown that starting materials of Ti, Cr, and C powders may be used to synthesize (Ti,Cr)C powder with a significant fraction of nanoparticles using the MA process. MA powders' microstructure has been characterized using XRD and TEM studies. With increasing micro-strain, milling for up to five hours caused the size of the

 doi:10.20944/preprints202212.0076.v1

crystallites to decrease to the nanoscale. Additionally, when MA time increases, the lattice parameter of (Ti,Cr)C solid solutions decreases. The average crystallite size, according to TEM examination, is about 15 nm, which is remarkably similar to the value obtained using the XRD approach. After 20 hours of milling, the amount of iron impurity increased due to milling medium abrasion. Therefore, this impurity had no effect on how (Ti,Cr)C carbide was formed. After spark plasma sintering of 5, 10 and 20 hours of the milled powders, XRD and SEM/EDX tests were made to learn and compare their phases and elemental distribution comparing to powder ones. Archimedes density tests and Rockwell Hardness (HRA) tests showed that 10 h milled cermet's physical properties were the worst with a value of 87.14 % and 83.2±1.7, respectively. 5 and 20 h cermets had relatively high physical properties comparing to 10 h one with over 98 % relative density and 93.3 ± 0.3 - 91.5 ± 0.4 hardness. Increasing milling time to 20 h also increased the corrosion resistance as it had 0.1270 ($\mu A/cm^{2)}$ I_{corr}, 395.63 ($k\Omega*cm^2$) R_p and 371.68 ($k\Omega*cm^2$).

Author Contributions: Conceptualization, M.M. and B.A.; methodology, M.M., I.E.D., B.A., F.S., N.J., and M.K.; validation, M.M., I.E.D., B.A., M.K., F.S., and N.J.; formal analysis, M.M., I.E.D., and B.A.; investigation, M.M., B.A., M.K., F.S., and N.J.; resources, M.M., I.E.D., and B.A.; data curation, M.M., I.E.D., and B.A.; writing—original draft preparation, M.M., I.E.D., B.A., and M.K.; writing—review and editing, M.M., I.E.D., B.A., M.K., F.S., and N.J.; visualization, M.M., I.E.D., B.A., M.K., F.S., and N.J.; project administration, M.M.; funding acquisition, M.M. I.E.D., and B.A. All authors have read and agreed to the published version of the manuscript.

Funding: This research received no external funding.

Institutional Review Board Statement: Not applicable.

Informed Consent Statement: Not applicable.

Data Availability Statement: Not applicable.

Conflicts of Interest: The authors declare no conflict of interest.

References

1. Mhadhbi, M.; Driss, M. Titanium Carbide: Synthesis, Properties and Applications. *BEN* **2021**, 2, 1-11.
2. Komratov, G.N. Oxidation Kinetics of Double Titanium-chromium Carbide and Chromium Carbide. *Poroshk. Metall*. **1999**, 9–10, 52–57.
3. Chen K.; Zhao L. Elastic Properties, Thermal Expansion Coefficients and Electronic Structures of $Ti_{0.75}X_{0.25}C$ Carbides. *J. Phys. Chem. Solids* **2007**, 68, 1805–1811.
4. Umanskii, A.P.; Lavrenko, V.A.; Chuprov, S.S.; Konoval, V.P. High-temperature Oxidation of Composites Based on Titanium Carbonitride and Double Titanium–chromium Carbide. *Nov. Ogneup.* **2006**, 8, 42–46.
5. Mhadhbi, M.; Polkowski, W. Synthesis and Characterization of Mechanically Alloyed Nanostructured (Ti,Cr)C Carbide for Cutting Tools Application. *Crystals* **2022**, 12, 1280.
6. Chuev, I.I.; Kovalev, D.Y. Effects of Titanium High-energy Ball Milling on The Solid-phase Reaction Ti+C. *Mater. Chem. Phys.* **2022**, 283, 126025.
7. Zhang, L.; Liang, Y.; Gu, J.; Yan, X.; Li, X.; Yu, P.; Wang, L. Synthesis of Nano (Ti,W)C Powder With Preferred Orientation and Twin Boundary Structure. *Adv. Powder Technol.* **2022**, 33, 103550.
8. Bandyopadhyay, S.; Dutta, H.; Pradhan, S.K. XRD and HRTEM Characterization of Mechanosynthesized $Ti_{0.9}W_{0.1}C$ Cermet. *J. Alloys Compd* **2013**, 581, 710–716.
9. Li, F.; Wang, W.; Dang, W.; Xu, Z.; Zhao, K.; Tang, Y. Microstructural Features and Oxidation Resistance of (Ti, Zr)C Solid Solution Nanofibers Fabricated Using Polymeric Precursors. *Ceram. Int.* **2019**, 45(18), 24941-24945.
10. Ke, D.; Pan, Y.; Wu, R.; Xu, Y.; Wang, P.; Wu, T. Effect of Initial Co Content on The Microstructure, Mechanical Properties and High-Temperature Oxidation Resistance of WCoB-TiC Ceramic Composites. *Ceram. Int.* **2018**, 44, 1213–1219.
11. Yung, D.L.; Maaten, B.; Antonov, M.; Hussainova, I. Oxidation of Spark Plasma Sintered ZrC-Mo and ZrC-TiC Composites. *Int. J. Refract. Metals Hard Mater*. **2017**, 66, 244–251.
12. Wang, Z.; Wang, J.; Xu, Y.; Yi, M.; Xiao, G.; Chen, Z.; Zhang, J.; Chen, H.; Xu, C. Microstructure and Mechanical Properties of (Ti,W)C Cermets Prepared By Ultrafast Spark Plasma Sintering. *Ceram. Int.* **2022**, 48(11), 15613-15621.
13. Zhang, Z.; Fu, S.; Aversano, F.; Bortolotti, M.; Zhang, H.; Hu, C.; Grasso, S. Arc Melting: A Novel Method to Prepare Homogeneous Solid Solutions of Transition Metal Carbides (Zr, Ta, Hf). *Ceram. Int.* **2019**, 45, 9316–9319.

14. Dutta, H.; Sen, A.; Bhattacharjee, J.; Pradhan, S.K. Preparation of Ternary $Ti_{0.9}Ni_{0.1}C$ Cermets by Mechanical Alloying: Microstructure Characterization by Rietveld Method and Electron Microscopy. *J. Alloys Comp.* **2010**, 493, 666–671.
15. Dutta, H.; Sen, A.; Pradhan, S.K.; Microstructure Characterization of Ball-mill Prepared Ternary $Ti_{0.9}Al_{0.1}C$ by X-ray Diffraction and Electron Microscopy. *J Alloys Comp.* **2010**, 501, 198–203.
16. Ghosh, B.; Pradhan, S.K. Microstructure Characterization of Nanocrystalline TiC Synthesized By Mechanical Alloying. *Mater. Chem. Phys*. **2010**, 120, 537–545.
17. Machio, C.; Nyabadza, D.; Sibanda, V.; Chikwanda, H.K. Characterization of Mechanically Alloyed fcc Ti-Mg-based Powders. *Powder Technol.* **2011**, 207(1-3), 387-395.
18. Ghosh, J.; Bysakh, S.; Mazumder, S. Multiphase Transformation and Hybrid Nanostructure Under Non-equilibrium and Equilibrium Condition During High-energy Ball Milling of $BaTiO_3$ Powders. *Ph. Transit.* **2014**, 87(4), 325-335.
19. El-Eskandarany, MS. Mechanical Alloying: For Fabrication of Advanced Engineering Materials. Norwich, New York, U.S.A: William Andrew Publishing; **2001**.
20. Rodriguez-Carvajal, J. Recent Advances in Magnetic Structure Determination By Neutron Powder Diffraction. *Phys. B* **1993**, 192, 55-69.
21. Rietveld, H.M. Line Profiles of Neutron Powder-Diffraction Peaks for Structure Refinement. *Acta Cryst.* **1967**, 22, 151–152.
22. Rietveld, H.M. A Profile Refinement Method for Nuclear and Magnetic Structures. *J. Appl. Cryst.* **1969**, 2, 65–71.
23. Wiles, D.B.; Young, R.A. A New Computer Program for Rietveld Analysis of X-ray Powder Diffraction Patterns. *J. Appl. Cryst*. **1981**, 14, 149–151.
24. Young, R.A.; Wiles, D.B. Profile Shape Functions in Rietveld Refinements. *J. Appl. Cryst*. **1982**, 15, 430–438.
25. Young, R.A. in: Young R.A. (Ed.), The Rietveld Method, Oxford University Press/IUCr, **1996**, pp. 1–38.
26. Lutterotti, L.; Scardi, P.; Maistrelli, P. LSI-a Computer Program for Simultaneous Refinement of Material Structure and Microstructure. *J. Appl. Cryst*. **1992**, 25, 459–462.
27. Ghosh, B.; Dutta, H.; Pradhan, S.K. Microstructure Characterization of Nanocrystalline Ni_3C Synthesized By High-energy Ball Milling. *J. Alloys Comp*. **2009**, 479, 193–200.
28. Warren, B.E. X-ray Diffraction, Chap. 13, Addison-Wesley, Reading, **1969**.
29. Zhao, Y.H.; Sheng, H.W.; Lu, K. Microstructure Evolution and Thermal Properties in Nanocrystalline Fe During Mechanical Attrition. *Acta Mater.* **2001**, 49, 365–375.
30. Oldfield, J.W. Electrochemical Theory of Galvanic Corrosion, STP978 Galvanic Corrosion. H.P. Hack Ed., ASTM Int. West Conshohocken, pp. 5–22, **1988**.
31. Nelson, E.E. Discussion of The Mechanism of Passivating-Type Inhibitors [M . Stern (pp. 638–647, Vol. 105)]. *J. Electro hem. Soc.* **1959**, 106(6) 540.
32. Luiz, L.A.; de Andrade, J.; Pesqueira, C.M.; Siqueira, I.B. de A.F.; Sucharski, G.B.; de Sousa, M.J. Corrosion Behavior and Galvanic Corrosion Resistance of WC and Cr_3C_2 Cermet Coatings in Madeira River Water. *J. Therm. Spray Technol.* **2021**, 30(1), 205–221.
33. Amini, M.; Rahimipour, M.R.; Tayebifard, S.A.; Palizdar, Y. Effect of Milling Time on XRD Phases and Microstructure of a Novel $Al_{67}Cu_{20}Fe_{10}B_3$ Quasicrystalline Alloy. *Mater. Res. Express* **2020**, 7, 065011.
34. Ponhan, K.; Tassenberg, K.; Weston, D.; Nicholls, K.G.M.; Thornton, R. Effect of SiC Nanoparticle Content and Milling Time on The Microstructural Characteristics and Properties of Mg-SiC Nanocomposites Synthesized with Powder Metallurgy Incorporating High-energy Ball Milling. *Ceram. Int*. **2020**, 46, 26956–26969.
35. Jabbari-Taleghani, M.A.; Torralba, J.M. Hot Workability of Nanocrystalline AZ91 Magnesium Alloy. *J. Alloys Compd*. **2014**, 595, 1–7.
36. Huang, J.Y.; Wu, Y.K.; Ye, H.Q. Ball Milling of Ductile Metals. *Mater. Sci. Eng. A* **1995**, 199, 165–172.
37. Mhadhbi, M.; Khitouni, M.; Escoda, L.; Suñol, J. J.; Dammak, M. Characterization of Mechanically Alloyed Nanocrystalline Fe(Al): Crystallite Size and Dislocation Density. *J. Nanomater.* **2010**, 712407, 8 pages.
38. Kamrani, S.; Penther, D.; Ghasemi, A.; Riedel, R.; Fleck, C. Microstructural Characterization of Mg-SiC Nanocomposite Synthesized by High Energy Ball Milling. *Adv. Powder Technol*. **2018**, 29, 1742–1748.
39. Zaara, K.; Chemingui, M.; Optasanu, V.; Khitouni, M. Solid Solution Evolution During Mechanical Alloying in Cu-Nb-Al Compounds. *Int. J. Miner. Metall. Mater*. **2019**, 26, 1129–1139.
40. Talischi, L.A.; Samadi, A. Structural Characterization and Ordering Transformation of Mechanically Alloyed Nanocrystalline Fe-28Al Powder. *J. Ultrafine Grained Nanostruct. Mater*. **2016**, 49, 112–119.
41. Ahamed, H.; Senthilkumar, V. Role of Nano-size Reinforcement and Milling on The Synthesis of Nano-crystalline Aluminium Alloy Composites by Mechanical Alloying. *J. Alloys Compd*. **2010**, 505, 772–782.
42. Koohkan, R.; Sharafi, S.; Shokrollahi, H.; Janghorban, K. Preparation of Nanocrystalline Fe–Ni Powders by Mechanical Alloying Used in Soft Magnetic Composites. *J. Magn. Magn. Mater.* **2008**, 320, 1089–1094.
43. Slimi, M.; Saurina, J.; Suñol, J.J.; Escoda, L.; Farid, M.; Greneche, J.M.; Khitouni, M. Mössbauer and X-ray Studies of Mechanically Alloyed $Fe_{60}Ni_{30}Cr_{10}$ Prepared By High Energy Ball Milling. *Adv. Powder Technol*. **2016**, 27, 1618–1624.
44. Matuła, I.; Zubko, M.; Dercz, G. Role of Sn as a Process Control Agent on Mechanical Alloying Behavior of Nanocrystalline Titanium Based Powders. *Mater*. **2020**, 13(9), 2110.
45. Salvo, C.; Aguilar, C.; Cardoso-Gil, R.; Medina, A.; Bejar, L.; Mangalaraja, R.V. Study on The Microstructural Evolution of Ti-Nb Based Alloy Obtained By High-energy Ball Milling. *J. Alloys Compd.* **2017**, 720, 254–263.

 doi:10.20944/preprints202212.0076.v1

46. Dercz, G.; Matuła, I.; Maszybrocka, J. Properties of Porous Ti-26Nb-6Mo-1.5Sn Alloy Produced Via Powder Metallurgy For Biomedical Application. *Phys MET Metallogr*. **2019**, 120, 1384–1391.
47. Dercz, G.; Pająk, L.; Formanek, B. Dispersion Analysis of NiAl-TiC-Al_2O_3 Composite Powder Ground in a High-energy Attritorial Mill. *J. Mater. Process. Technol.* **2006**, 175, 334–337.
48. Chen, Y.; Hu, Z.; Xu, Y.; Wang, J.; Schützendübe, P.; Huang, Y.; Liu, Y.; Wang, Z. Microstructure Evolution and Interface Structure of Al-40wt%Si Composites Produced by High-energy Ball Milling. *J. Mater. Sci. Technol.* **2019**, 35(4), 512-519.
49. Hajalilou, A.; Kianvash, A.; Lavvafi, H.; Shameli, K. Nanostructured Soft Magnetic Materials Synthesized Via Mechanical Alloying: A Review. *J. Mater. Sci. Mater. Electron*. **2018**, 29(2), 1690-1717.
50. Kunrath, A.O.; Reimanis, I.E.; Moore, J.J. Microstructural Evolution of Titanium Carbide–Chromium Carbide (TiC–Cr_3C_2) Composites Produced Via Combustion Synthesis. *J. Am. Ceram. Soc.* **2002**, 85(5), 1285-1290.
51. Shankar, E.; Prabu, S.B.; Padmanabhan, K.A. Mechanical Properties and Microstructures of TiCN/nano-TiB_2/TiN Cermets Prepared by Spark Plasma Sintering. *Ceram. Int.* **2018**, 44(8), 9384–9394.
52. Feng, P.; Xiong, W.; Yu, L.; Zheng, Y.; Xia, Y. Phase Evolution and Microstructure Characteristics of Ultrafine Ti(C,N)-based Cermet by Spark Plasma Sintering. *Int. J. Refract. Met. Hard Mater.* **2004**, 22(2), 133–138.
53. Soundaraj, P.V.; Sembulingam, S.S.; Shanmugavel, B.P. On the Role of B_4C on Hardness and Toughness of TiCN-SiC-TiN-Cr_3C_2-Co Cermet. *Int. J. Refract. Met. Hard Mater.* **2020**, 90, 105252.
54. H. Xiong, Y. Guo, Z. Li, K. Zhou, New Production of (Ti, W)C-based Cermets Toughened By In-situ Formed WC and Twinned (Ti, W)C Platelets: Carbonization of The Nix($Ti_{0.6}$, $W_{0.4}$)4C-type η Phases. *J. Alloys Compd.* **2018**, 731, 253–263.
55. Zhang, L.; Ling, Q.; Gu, J.; Zhong, Z.; Long, J.; Wang, C. Strengthening and Toughening of Ti(C,N)-based Cermets: (Ti,W)C Additive Design and The Mechanism. *Int. J. Refract. Met. Hard Mater.* **2022**, 103, 105758.
56. Wan, W.; Xiong, J.; Yang, M.; Guo, Z.; Dong, G.; Yi, C. Effects of Cr_3C_2 Addition on The Corrosion Behavior of Ti(C, N)-based Cermets. *Int. J. Refract. Met. Hard Mater.* **2012**, 31, 179–186.
57. Chen, S.; Xiong, W.; Yao, Z.; Zhang, G.; Chen, X.; Huang, B.; Yang, Q. Corrosion Behavior of Ti(C,N)-Ni/Cr Cermets in H_2SO_4 Solution. *Int. J. Refract. Met. Hard Mater.* **2014**, 47, 139–144.
58. Vorotilo, S.; Kiryukhantsev-Korneev, P.V.; Seplyarskii, B.S.; Kochetkov, R.A.; Abzalov, N.I.; Kovalev, I.D.; Lisina, T.G.; Zaitsev, A.A. (Ti,Cr)C-Based Cermets with Varied Nicr Binder Content via Elemental SHS for Perspective Cutting Tools. *Crystals* **2020**, 10(5), 412.
59. Kong, D.; Dong, C.; Ni, X.; Li, X. Corrosion of Metallic Materials Fabricated By Selective Laser Melting. *npj Mater. Degrad.* **2019**, 3(1), 24.
60. He, L.; Gao, Y.; Li, Y.; Liu, Z.; Huo, X.; Zhai, W. Effect of Milling Time on Powder's Structure Evolution of Ti(C,N)-304 Stainless Steel Cermet. *Mater. Res. Express* **2018**, 5(3), 36516.